Image Stabilization of a Model-Following Dual-Stage System With Charge-Coupled Device Measurement

Yun Wu, Liangzong Zhang, and Tao Tang, *Senior Member, IEEE*

***Abstract*—This article develops a charge couple device (CCD)-based dual-stage system consisting of cubic Stewart platform and tip-tilt mirror to stabilize the line-of-sight (LOS) for space optical payloads. Due to the conventional offloading strategy needing the accurate characteristic of the CCD and additional position sensor in terms of precision and bandwidth, a novel model-following offloading strategy is presented to achieve the offloading for the dual-stage system. The essence of the proposed strategy is that the following position signal can be estimated through combining the controller output with the model-based estimation of the tip-tilt mirror to be offloaded into the Stewart platform. Besides, an error-based observation control technique is introduced to relax the limitations imposed by the low sampling rate of the CCD on closed-loop performance for the tip-tilt mirror loop. This technique reduces reliance on the precise control model and optimizes the tracking performance by the design of an appropriate Q-filter. The simulations and experiments of the dual-stage image stabilization system demonstrate the validity of the presented approach.**

***Index Terms*—Charge couple device, model-based estimation, dual-stage system, Stewart platform, tip-tilt mirror.**

I. Introduction

AS THE stability and pointing requirements for space optical payloads get more stringent, isolating from microvibrations to prevent the deterioration of the sensitive optical payload performance becomes more critical [1]. A common configuration for vibration rejection and precision pointing of space optical payloads is the Stewart platform. The platform has six degrees of freedom where six active struts are adjusted to suppress the disturbance and track a trajectory [2], [3], [4], [5], [6]. Various vibration rejection and pointing control systems have been developed [7], [8], [9]. For example Thayer designed a unique hexapod for the active isolation and pointing control of space-based systems, featured by the very soft axial stiffness (3 Hz corner frequency). [8]. A vibration isolation and dual-stage actuation pointing system based on a soft Stewart platform is developed for space precision payloads [9]. However, there exists a fundamental trade-off of bandwidth between vibration isolation and pointing in the design of a Stewart platform control system, which prevents achieving high-precision tracking.

Dual-stage control is the most effective way to achieve high levels of tracking accuracy for control systems, a large number of dual-stage pointing control systems have been proposed [10], [11], [12], [13], [14], [15]. A composite axis control system comprised of a gimbaled mirror and a piezoelectric fast steering mirror (FSM) is developed to solve the pointing jitter problem of the electro-optical platform in complex airborne vibration environment [11], [12]. The results demonstrate a 93% reduction in the pointing jitter of the optical axis. A ATP compound axis control system is presented in [13], effectively improving the tracking precision for the intersatellite optical communication system. The simulation results show that the tracking precision of the system is less than $2\mu rad$. Based on the dual-stage control concept, some scholars propose combining the Stewart platform with a high-bandwidth tip-tilt mirror to form a dual-stage system. A dual-stage robust high precision pointing control system consisting of the Stewart platform and the FSM is studied for a mid-class space coronagraphic observatory [14]. The Stewart platform stabilizes the telescope line-of-sight (LOS) to 1 mas in both pitch and yaw axes. The FSM further centers the star to 0.1 mas. In [15], a two-stage vibration suppression and precision pointing system is proposed for space optical payloads, comprising a piezoelectric-based Stewart platform and a FSM subsystem. The Stewart platform is applied to reject the high-frequency structural vibrations, and the FSM is used to compensate the residual low-frequency jitters. Ref. [16] presented a two-stage control system based on the Stewart platform to ensure the stabilization and pointing requirements for space telescope. The above-mentioned dual-stage systems are either dual-detector or single-detector types. Dual-detector types have no coupling between the two stages but require a greater number of sensors, while single-detector types have fewer sensors but require the design of a decoupling link. Additionally, the position information of the fine stage needs to be offloaded to the coarse stage, introducing measurement errors.

Based on the above research status, this article develops a dual-stage image stabilization system based on the model-following offloading strategy for the vibration isolation and high-precision pointing of space optical payloads, which starts with a Stewart platform that provides vibration suppression capability, and is augmented with a tip-tilt mirror. The essence of the model-following offloading strategy is that the following position signal can be estimated through combining the controller output with the model-based estimation of the tip-tilt mirror,

Manuscript received 11 April 2024; accepted 16 April 2024. Date of publication 19 April 2024; date of current version 24 June 2024. This work was supported in part by the National Natural Science Foundation of China under Grant 62375267 and in part by Sichuan Province Science and Technology Support Program under Grant 2021JDJQ0028. *(Corresponding author: Tao Tang.)*

The authors are with the National Key Laboratory of Optical Field Manipulation Science and Technology, the Key Laboratory of Optical Engineering, Chinese Academy of Sciences, Chengdu 610209, China, and also with the Institute of Optics and Electronics, Chinese Academy of Science, Chengdu 610209, China (e-mail: taotang@ioe.ac.cn).

Digital Object Identifier 10.1109/JPHOT.2024.3391229

which is offloaded onto the Stewart platform. Therefore, the reliance on additional position sensors is reduced. Besides, The strategy fully leverages the benefits of the high bandwidth control model, which reduces the difficulty of system decoupling. Since the well-closed-loop performance is usually hindered by the finite sampling rate in the CCD-based tip-tilt mirror loop of the dual-stage system [10], a variety of control methods have been presented to decrease the adverse effects of time delay and, thus, improve the tracking performance [17], [18], [19], [20], [21], [22], [23], [24], [25], [26].

The model-based feedforward control with no high bandwidth required proves to be an effective approach to optimize the closed-loop performance if the target trajectory and accurate control model can be obtained. Extra sensors such as encoders and gyros are introduced to synthesize target information, which is then further processed to obtain higher-order information through predictive filtering algorithms. The target information is then fed forward into the feedback loop. Obviously, this approach is limited by sensor performance and filtering algorithms [24], [25]. An improved Smith predictor in [26] is capable of compensating for the time delay in the CCD-based control systems. The underlying principle is that the high-speed gyro information is integrated to add into the feedback position loop. However, the predictor is highly sensitive to discrepancies between the reality and model, and the low-frequency drift of the gyro must be considered in a real space environment. This article presented an error-based observation feedforward control method to improve the tracking performance of the tip-tilt mirror control subsystem. The method assists the original CCD-based feedback loop by only utilizing the LOS error to generate a compensator. Since the original error attenuation function is multiplied by 1-Q (Q is the designed filter), minimization of tracking error is transformed into optimizing the Q-filter. A design criterion that compromises between tracking performance and closed-loop stability is developed for the Q-filter. This method relaxes the constraints on an accurate model and does not require extra sensors in comparison to existing feedforward control strategies.

Our work has following major contributions:

- We introduce a high-bandwidth tip-tilt mirror to resolve the contradiction between the vibration isolation performance and tracking accuracy of the Stewart platform, achieving high-precision tracking under good vibration isolation performance.
- We propose a model-following offloading strategy that fully leverages the benefits of the high bandwidth control model of the tip-tilt mirror for the dual-stage image stabilization system. Compared with the conventional position-signal offloading strategy, the proposed strategy reduces the difficulty of system decoupling. As long as the bandwidth of the fine stage is much larger than that of the coarse stage, the system is decoupled. Additionally, it reduces reliance on additional position sensors, avoiding decreases in tracking accuracy due to measurement errors.
- An error-based observation control method is presented to enhance the tracking accuracy of CCD-based tip-tilt control subsystem by designing of an appropriate Q-filter. This method relaxes the constraint on accurate model and eliminates the requirement for extra sensors.

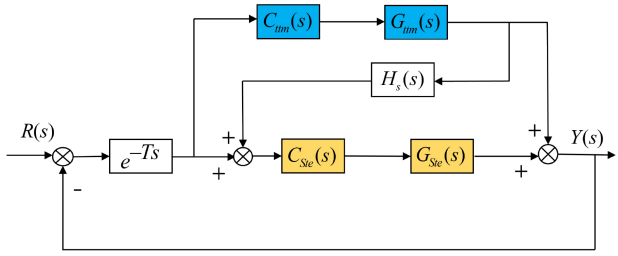

Fig. 1. The control structure of the dual-stage control system based on position signal-based offloading strategy.

The remainder of this article is organized as follows. Section II presents a detailed analysis of two types of offloading strategies, including the position signal-based offloading strategy and the model-following offloading strategy. Section III designs control schemes for the CCD-based Stewart platform subsystem and tip-tilt mirror subsystem. The error-based observation feedforward control method is introduced, mainly describing the implementation process, the performance analysis, and the parameter design of Q-filter. In Section IV, the simulation and analysis is presented. Section V conducts the experiments to verify the proposed approach, and the experimental results are discussed. Concluding remarks are given in Section VI.

II. The Offloading Strategy of the Dual-Stage Image Stabilization System System

This section presents two types of offloading strategies for the dual-stage image stabilization system, including the position signal-based offloading strategy and the model-following offloading strategy.

A. The Position Signal-Based Offloading Strategy

The conventional dual-stage control system adopts the position signal-based offloading strategy to implement the offloading control, and the control structure is illustrated in Fig. 1. $R(s)$ represents the reference position information. $Y(s)$ is the output information of the system. e^{-Ts} represents the time delay of the CCD. $H_s(s)$ is the decoupling controller. $G_{ttm}(s)$ and $G_{Ste}(s)$ are the control models of the fine subsystem (tip-tilt mirror) and the coarse subsystem (Stewart platform), respectively. $C_{ttm}(s)$ and $C_{Ste}(s)$ are the position controllers of the fine subsystem and the coarse subsystem, respectively. Defining $M_f(s) = C_{ttm}(s)G_{ttm}(s)$ and $M_c(s) = C_{Ste}(s)G_{Ste}(s)$. The closed-loop transfer function depicted in Fig. 1 is as follows:

$$G_{close}(s) = \frac{(M_f(s) + M_c(s) + M_f(s)M_c(s)H_s(s))e^{-Ts}}{[1 + M_f(s)e^{-Ts}]\,[1 + M_c(s)e^{-Ts}] + U} \tag{1}$$

where $U = e^{-Ts}M_f(s)M_c(s)(H_s(s) - e^{-Ts})$. It can be seen from (1) that the stability of the system is affected by the decoupling controller $H_s(s)$. The condition for the system to

be a static autonomous system is

$$H_s(s) = e^{-Ts} \tag{2}$$

Combining (1) and (2) yields

$$G_{close}(s) = \frac{(M_f(s) + M_c(s) + M_f(s)M_c(s)H_s(s))e^{-Ts}}{[1 + M_f(s)e^{-Ts}]\,[1 + M_c(s)e^{-Ts}]} \tag{3}$$

Since $1 + M_c(s)e^{-Ts}$ and $1 + M_f(s)e^{-Ts}$ are the characteristic polynomials of the coarse subsystem and fine subsystem, respectively, the closed-loop stability of the dual-stage system can be guaranteed if both coarse subsystem and fine subsystem are stable. From (1), the error attenuation function illustrated in Fig. 1 is depicted below.

$$E(s) = \frac{1}{[1 + M_f(s)e^{-Ts}][1 + M_c(s)e^{-Ts}] + U} \tag{4}$$

When the system is static autonomous, (4) is rewritten as

$$E(s) = \frac{1}{[1 + M_f(s)e^{-Ts}][1 + M_c(s)e^{-Ts}]} = E_f(s)E_c(s) \tag{5}$$

Here, $E_c(s) = 1/[1 + M_c(s)e^{-Ts}]$ and $E_f(s) = 1/[1 + M_f(s)e^{-Ts}]$ represent error suppression functions of coarse subsystem and fine subsystem, respectively. Based on (5), the indiscrimination degree of the dual-stage system is the sum of indiscrimination degree of the coarse subsystem and the fine subsystem. Therefore, the dual-stage system has a significant improvement in the tracking accuracy compared to the single-stage system. However, constructing an accurate characterization of the CCD is challenging due to the severe nonlinear behavior, which may destroy the system stability. Besides, additional sensors are required to measure the position of the fine subsystem so as to generate the input signal for controlling the coarse subsystem. Thus a model-following offloading strategy built upon the original strategy is proposed in the following subsection to overcome these difficulties.

B. The Model-Following Offloading Strategy

The control structure of the dual-stage system based on the model-following offloading strategy is depicted in Fig. 1. $\hat{G}_{ttm}(s)$ represents the estimation of the control model $G_{ttm}(s)$. As we can see, the strategy generates the following position signal by combining the controller output with the model-based estimation of the fine subsystem, which is offloaded into the coarse subsystem. Therefore, extra position sensors are not required. The closed-loop transfer function illustrated in Fig. 2 is given as follows (the dotted line means non-existence):

$$\begin{aligned}\bar{G}_{close}(s) &= \frac{(M_f(s) + \bar{M}_f(s)M_c(s))e^{-Ts}}{1 + (M_f(s) + \bar{M}_f(s)M_c(s))e^{-Ts}} \\ &= \frac{(M_f(s) + \bar{M}_f(s)M_c(s))e^{-Ts}}{[1 + M_f(s)e^{-Ts}]\,[1 + \bar{G}_f(s)M_c(s)e^{-Ts}]}\end{aligned} \tag{6}$$

where, $\bar{G}_f(s) = \bar{M}_f(s)/[(1 + M_f(s))e^{-Ts}]$, $\bar{M}_f(S) = C_{ttm}(s)\hat{G}_{ttm}(s)$. Let $L_c(s) = 1 + M_c(s)e^{-Ts}$ and $L_c'(s) = 1 + \bar{G}_f(s)M_c(s)e^{-TS}$, the zero-pole expressions

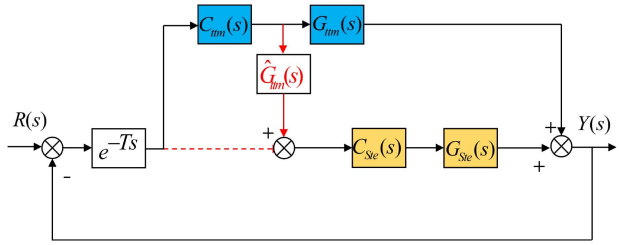

Fig. 2. The control structure of dual-stage control system based on model-following offloading strategy.

of $L_c(s)$ and $L_c{}'(s)$ are depicted below.

$$\begin{cases} L_c(s) = \frac{\prod_{i=1}^{n}(s+p_i)}{\prod_{j=1}^{n}(s+q_j)} \\ L'_c(s) = \frac{\prod_{i=1}^{n}(s+p_i+\varepsilon_i)\prod_{a=n+1}^{N}(s+p_a)}{\prod_{j=1}^{m}(s+q_j+\lambda_j)\prod_{b=m+1}^{M}(s+q_b)} \end{cases} \tag{7}$$

Here, $p_i (i \in (1, n))$ and $q_j (j \in (1, m))$ are zeros and poles of $L_c(s)$, respectively. The introduction of $\varepsilon_i (i \in (1, n))$ and $\lambda_j (j \in (1, m))$ brought by $\bar{G}_f(s)$ causes changes in p_i and q_j. Compared to $L_c(s)$, $p_a (a \in (n + 1, N))$ and $q_b (a \in (m + 1, M))$ are the added zeros and poles, respectively. From (7), the condition for equation $L_c{}'(s) = l_c(s)$ to hold is

$$\begin{cases} \varepsilon_i \to 0, \text{ in all } i \in (1, n) \\ \lambda_j \to 0, \text{ in all } i \in (1, m) \\ \min(q_b) \gg \max(q_j), b \in (m + 1, M) \\ \frac{\prod_{a=n+1}^{N}(s+p_a)}{\prod_{b=m+1}^{M}(s+q_b)} \approx 1 \end{cases} \tag{8}$$

Combining (6) and (8) yields

$$\bar{G}_{close}(s) = \frac{(M_f(s) + \bar{M}_f(s)M_c(s))e^{-Ts}}{[1 + M_f(s)e^{-Ts}][1 + M_c(s)e^{-Ts}]} \tag{9}$$

According to (9), the stability of both the coarse subsystem and the fine subsystem ensures the closed-loop stability of the dual-stage system. The dual-stage system is statically autonomous. From the frequency domain viewpoint, the bandwidth of $\bar{G}_f(s)$ needs to be much higher than that of $M_c(s)e^{-Ts}$ to obtain (9). Since the bandwidth of $\bar{G}_f(s)$ is greater than the closed-loop bandwidth of the fine subsystem, and the bandwidth of $M_c(s)e^{-Ts}$ is smaller than the closed-loop bandwidth of the coarse subsystem, then (9) holds if

$$\frac{w_f}{w_c} \gg 1 \tag{10}$$

where, w_f and w_c are the closed-loop cutoff frequencies of the fine subsystem and the coarse subsystem, respectively. As a result, the closed-loop bandwidth of the fine subsystem must be much higher than that of the coarse subsystem to be statically autonomous for the dual-stage system.

Further analyze the stability of the dual-stage control system. In order to facilitate the analysis, let $\bar{M}_f(s) = M_f(s)$ and ignore the time delay e^{-Ts}. It can be seen from (6) that the open-loop transfer function is

$$\begin{aligned}\bar{G}_{open}(s) &= (M_f(s) + \bar{M}_f(s)M_c(s))e^{-Ts} \\ &\approx M_f(s) + M_f(s)M_c(s)\end{aligned} \tag{11}$$

Let $F(s) = \frac{M_c(s)}{1+M_c(s)}$, rewriting (11) yields

$$\bar{G}_{open}(s) = \frac{M_c(s) \times M_f(s)}{F(s)} \tag{12}$$

Let

$$A(w) = \frac{w}{w'_c} \tag{13}$$

Where w'_c is the open-loop cutoff frequency of the coarse subsystem. When $A(w)$ is small, $M_c(s) \geqslant 1$, and $F(s) = 1$. When $A(w)$ is large, $M_c(s) \leqslant 1$, and $F(s) = M_c(s)$. Thus, the open-loop transfer function of the dual-stage system can be deduced

$$\begin{cases} \bar{G}_{open}(s) \approx M_c(s) \times M_f(s) (\text{low frequency band}) \\ \bar{G}_{open}(s) \approx M_f(s) (\text{medium - high frequency band}) \end{cases} \tag{14}$$

Clearly, the stability of the dual-stage control system is consistent with the stability of the fine subsystem in the medium-high frequency band. Thus, when $\frac{w'_f}{w'_c} \geqslant 1$ (w'_f is the open-loop cutoff frequency of the fine subsystem), the dual-stage control system has enough closed-loop stability margin.

The control mode of the fine subsystem usually has high linear and high bandwidth. Let w_{of} is the cutoff frequency of the control model $G_{ttm}(s)$, we have

$$\frac{w_{of}}{w_f} \geqslant 1 \tag{15}$$

Thus, the high-bandwidth control model can be regarded as 1 in the low-frequency band, we have

$$\hat{G}_{ttm}(jw) \approx 1, w \in (0, w_c) \tag{16}$$

It is obvious that the difficulty of system decoupling is reduced, and the controller output of the fine subsystem can be directly offloaded to the coarse subsystem.

From (6), the error attenuation function in Fig. 1 is given as

$$\bar{E}(s) = \frac{1}{\left[1 + M_f(s)e^{-Ts}\right]\left[1 + \bar{G}_f(s)M_c(s)e^{-Ts}\right]} \tag{17}$$

Substituting (10) into (17) yields

$$\bar{E}(s) \approx \frac{1}{\left[1 + M_f(s)e^{-Ts}\right]\left[1 + M_c(s)e^{-Ts}\right]} = E(s) \tag{18}$$

According to (18), both offloading strategies exhibit the same enhancement in error attenuation capability. In contrast to the position signal-based offloading strategy, the model-following offloading strategy reduces the difficulty of system decoupling by leveraging the advantage of the high bandwidth of the control model. Moreover, it eliminates the need for extra position sensors by utilizing the controller output to offload the fine subsystem. Obviously, the model-following offloading strategy is a significant improvement over the position signal-based offloading strategy.

III. The Design of the CCD-Based Dual-Stage Closed-Loop System

In this section, we design the CCD-based Stewart platform control subsystem and the CCD-based tip-tilt mirror control subsystem.

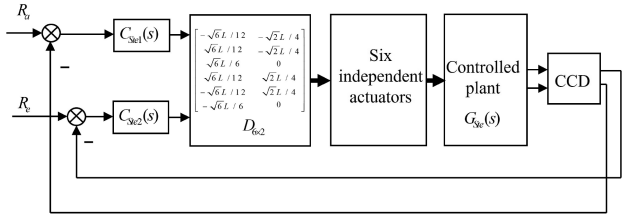

Fig. 3. The control scheme of the CCD-based Stewart platform subsystem.

A. The Design of the CCD-Based Stewart Platform Control Subsystem

The fundamental control scheme for the CCD-based Stewart platform tracking subsystem is to decouple the multiple-input-multiple-output (MIMO) control into the single-input-single-output (SISO) control using the Jacobi matrix J_s [27]. Since the motion of the optical axis is only related to the azimuth and elevation axes of the Stewart platform, the decoupled CCD-based tracking control scheme is illustrated in Fig. 3. R_a and R_e represent the reference positions of the azimuth and elevation axes, respectively. $D_{6\times2}$ is the decoupling matrix and consists of the columns of J_s corresponding to the azimuth and elevation axes [28]. $C_{Ste1}(s)$ and $C_{Ste2}(s)$ are the controllers. From Fig. 3, the outputs from $C_{Ste1}(s)$ and $C_{Ste2}(s)$ are decomposed by $D_{6\times2}$ to command the actuators of six struts.

B. The Design of the CCD-Based Tip-Tilt Mirror Control Subsystem

1) The Conventional Control: The conventional control structure of the CCD-based tip-tilt mirror control subsystem is a feedback loop, which mainly consists of the controlled plant of the tip-tilt mirror $G_{ttm}(s)$, the position controller $C_{ttm}(s)$, and the time delay e^{-Ts}. The error attenuation function of the control system is expressed as

$$\bar{S} = \frac{1}{1 + G_{ttm}(s)C_{ttm}(s)e^{-Ts}} \tag{19}$$

According to (19), the closed-loop performance is determined by the time delay e^{-Ts} if the controlled plant $G_{ttm}(s)$ is fixed, which limits the control gain. The integral controller $C_{ttm}(s) = K/s$ is a perfect choice for the control system with time delay. Considering the constraints of phase margin (PM) greater than 45 degrees and gain margin (GM) greater than 6 dB, the cutoff frequency w_c of the open-loop transfer function $G_{of} = C_{ttm}(s)G_{ttm}(s)e^{-Ts}$ and the integral gain K can be easily derived that $K = w_c = \frac{\pi}{4T}$. Because the open-loop characteristic of the controlled plant $G_{ttm}(s)$ can be approximated as 1 in the low-frequency range due to a high natural frequency up to hundreds of Hz, rewrite (19) as

$$\bar{S} = \frac{1}{1 + \frac{\pi}{4T}\frac{1}{s}e^{-Ts}} \tag{20}$$

Based on (20), $|\bar{S}(jw)|_{w_k} = \sqrt{2}/2$ results in $w_k = \frac{\sqrt{2}\pi}{4T}$, which is the bandwidth of the error attenuation function. Therefore, the control performance of the tip-tilt mirror is constrained

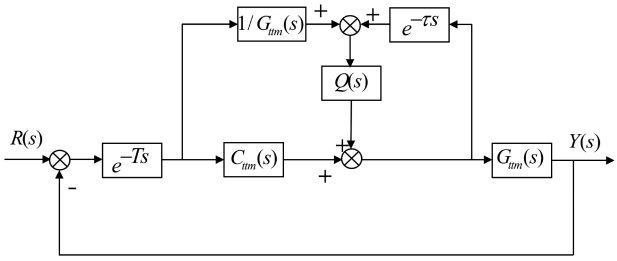

Fig. 4. The control structure of the proposed error-based observation.

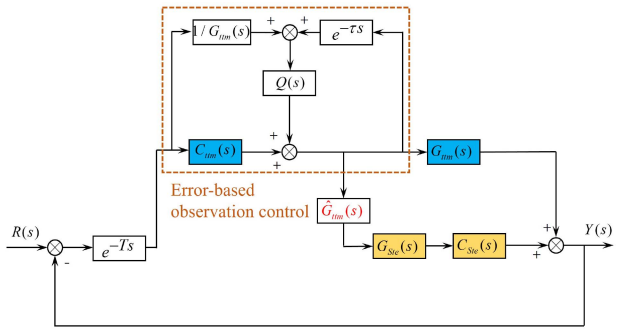

Fig. 5. The control structure of the dual-stage image stabilization system.

by the time delay of the CCD. However, long exposure times of the CCD are required to achieve a high signal-to-noise ratio beneficial to image quality. Thus, low sampling rate and time delay are unavoidable in the CCD-based control system to hinder a good closed-loop performance.

2) The Error-Based Observation Control: An error-based observation control method is proposed to relax the restraint on the time delay for the tip-tilt mirror control subsystem, the essence of which is a type of repetitive control [29], [30]. The control structure of the proposed error-based observation is shown in Fig. 4, where $1/G_{ttm}(s)$ represents the approximate inverse of the controlled plant, $e^{-\tau s}$ is the estimation of the time delay, and $Q(s)$ is the designed filter. Therefore, the control structure of the dual-stage image stabilization system in this article is given in Fig. 5. The error attenuation function illustrated in Fig. 4 is as follows:

$$S = \frac{1 - e^{-Ts}Q(s)}{1 + C_{ttm}(s)G_{ttm}(s)e^{-\tau s} + \lambda} \tag{21}$$

Where $\lambda = (e^{-\tau s}G_{ttm}(s){G^{-1}}_{ttm}(s) - e^{-Ts})Q(s)$. If $(e^{-\tau s}G_{ttm}(s){G^{-1}}_{ttm}(s) - e^{-Ts})Q(s) \approx 0$ is satisfied, due to $S \approx (1 - e^{-Ts}Q(s))\bar{S}$, if $(e^{-\tau s}G_{ttm}(s){G^{-1}}_{ttm}(s) - e^{-Ts})Q(s) \approx 0$, the closed-loop performance of the system can be effectively improved by minimizing $1 - e^{-\tau s}Q(s)$. As a result, the key task of the error-based observation control is how to optimize the $Q(s)$. It is practically impossible to arrive at $e^{-\tau s}G_{ttm}(s){G^{-1}}_{ttm}(s) - e^{-Ts} \approx 0$ in the high frequencies due to the uncertainty in the high-frequency model of $G_{ttm}(s)$. Thus $Q(s)$ needs to feature low-pass characteristics to reduce the damage of unmodeled dynamics so as to make $(e^{-\tau s}G_{ttm}(s){G^{-1}}_{ttm}(s) - e^{-Ts})Q(s)$ close to zero. From the closed-loop performance's perspective, $Q(s)$ should have as high a bandwidth as possible. However, the case is opposite against the system stability

a) Stability analysis: The closed-loop transfer function illustrated in Fig. 5 is expressed as

$$\hat{G}_{close}(s) = \frac{C_{ttm}(s)G_{ttm}(s)e^{-\tau s} + Q(s)M(s)}{1 + C_{ttm}(s)G_{ttm}(s)e^{-\tau s} + (M(s) - e^{-Ts})\,Q(s)} \tag{22}$$

Here, $M(s) = e^{-\tau s}G^{-1}_{ttm}(s)G_{ttm}(s)$. In order to ensure the stability of the system, the poles of $\hat{G}_{closed}(s)$ must all be in the left half of the complex plane. The corresponding characteristic polynomial $J(s)$ is as follows:

$$\begin{aligned} J(s) &= 1 + C_{ttm}(s)G_{ttm}(s)e^{-\tau s} + [M(s) - e^{-Ts}]Q(s) \\ &= (1 + C_{ttm}(s)G_{ttm}(s)e^{-\tau s}) \times (1 + T(s)) \end{aligned} \tag{23}$$

where, $T(s) = \frac{(e^{-\tau s}G^{-1}_{ttm}(s)G_{ttm}(s) - e^{-Ts})Q(s)}{1 + C_{ttm}(s)G_{ttm}(s)e^{-\tau s}}$. As the original feedback loop is stable, the stability of the closed-loop system depends on $1 + T(s)$. According to the small gain theorem, $T(s)$ needs to meet the condition in (24)

$$|T(s)|_\infty = \left| \frac{(e^{-\tau s}{G^{-1}}_{ttm}(s)G_{ttm}(s) - e^{-Ts})Q(s)}{1 + C_{ttm}(s)G_{ttm}(s)e^{-\tau s}} \right|_\infty < 1 \tag{24}$$

Here, $1/[1 + C_{ttm}(s)G_{ttm}(s)e^{-\tau s}]$ is a high-pass filter. $(e^{-\tau s}{G^{-1}}_{ttm}(s)G_{ttm}(s) - e^{-Ts})$ is very close to zero below the frequency at which an accurate plant model can be obtained. Thus, (24) can be met if the following condition is satisfied (bd is short for bandwidth):

$$bd(Q(s)) < \min bd\left\{ e^{-\tau s}G^{-1}_{ttm}(s)G_{ttm}(s) - e^{-Ts}, \frac{1}{1 + C_{ttm}(s)G_{ttm}(s)e^{-\tau s}} \right\} \tag{25}$$

It is shown that the bandwidth of $Q(s)$ must not exceed that of any of $e^{-\tau s}G^{-1}_{ttm}(s)G_{ttm}(s) - e^{-Ts}$ and $\frac{1}{1+C_{ttm}(s)G_{ttm}(s)e^{-\tau s}}$. However, the criterion of (25) does not take into account the phase condition. To make the introduced error-based observation controller does not effect the stability of the system, the phase margin of the open-loop transfer function $G'_{of}(s) = C_e(s)G_{ttm}(s)$ should be enough. Here, $C_e(s)$ is expressed as

$$C_e(s) = \frac{C_{ttm}(s) + Q(s)G^{-1}_{ttm}(s)e^{-Ts}}{1 - Q(s)e^{-\tau s}} = M_1(s)M_2(s) \tag{26}$$

Where, $M_1(s) = \frac{C_{ttm}(s)G_{ttm}(s) + e^{-Ts}Q(s)}{C_{ttm}(s)G_{ttm}(s)}$ and $M_2(s) = \frac{C_{ttm}(s)}{1 - e^{\tau s}Q(s)}$. The first term M_1 is approximated as the inverse of the closed-loop transfer function, and is very close to unit one below the bandwidth of $e^{-\tau s}Q(s)$ or in the high-frequency range if $|e^{-\tau s}Q(s)|_\infty \leq |C_{ttm}(s)G_{ttm}(s)|_\infty$. Therefore the major characteristic of the open-loop transfer function $G'_{of}(s)$ is determined by M_2 due to $M_1 \approx 1$. The constraint shown in (27) needs to be satisfied in order to guarantee the closed-loop stability.

$$\arg\,[K(jw)] > 0 \tag{27}$$

Here, $K(s)=\frac{1}{1-e^{-\tau s}Q(s)}$. In summary, $Q(s)$ should be designed to minimize $1-e^{-\tau s}Q(s)$ as much as possible when (25) and (27) are met.

b) Q-filter design: The filter $Q(s)$ should feature low-pass characteristics, which can decrease the destruction of high-frequency non modeling characteristics on the closed-loop stability. A common low-pass filter is expressed as

$$Q(s)=\frac{\sum_{k=1}^{m-2}C_m^k(\varsigma s)^k+1}{(\varsigma s+1)^m} \tag{28}$$

Here, m is the order, and ς is a tuning parameter that approximately determines the bandwidth of the low-pass filter. Substituting $e^{-\tau s}=1+\frac{1}{i!}\sum_{i=1}^{\infty}(-\tau s)^i$ into $K(s)$ yields

$$K(s)=\frac{1}{1-e^{-\tau s}Q(s)}=\frac{(\varsigma s+1)^m}{(\varsigma s)^m+(\varsigma s)^{m-1}+\phi} \tag{29}$$

Where, $\phi=\frac{1}{i!}\sum_{i=1}^{\infty}(-\tau s)^i\left[\sum_{k=2}^{m-2}C_m^k(\varsigma s)^k+1\right]$. There are more than two pure differentiators for the denominator of $K(s)$, which means that it has larger than 180° phase loss at low frequencies until closing to the cut-off frequency. From the Bode diagram, the phase margin of the open-loop transfer function with error-based observation control G'_{of} will be less than zero, leading to the closed-loop system instability. From the phase margin's perspective, the condition for the system being stable is that (27) must be achieved. Ignoring the term $\phi=\frac{1}{i!}\sum_{i=1}^{\infty}(-\tau s)^i\left[\sum_{k=2}^{m-2}C_m^k(\varsigma s)^k+1\right]$, the phase condition of the system is easily derived below.

$$(m)\arctan(\varsigma w_c)>\frac{\pi(m-1)}{2} \tag{30}$$

Based on (30), it can be seen that the cut-off frequency $1/\varsigma$ of $Q(s)$ decreases with the increasing order m. Compared to the original feedback loop, the enhancement of the closed-loop performance with the error-based observation control is expressed below

$$\frac{1}{K(s)}=\frac{(\varsigma s)^m+(\varsigma s)^{m-1}+\phi}{(\varsigma s+1)^m} \tag{31}$$

As is seen from (31), the closed-loop performance can be improved by increasing the bandwidth and the order of $Q(s)$. Unfortunately, excessive bandwidth and order of $Q(s)$ will destroy the phase condition expressed in (30), leading to system instability. Therefore, the design of $Q(s)$ filter must be with a compromise between tracking performance and closed-loop stability. As a matter of fact, the low-frequency performance is enhanced by more than 20 dB as the order increases by one, while the bandwidth of $1/K(s)$ reduces. Compared with the high order, the low order can obtain high-bandwidth error attenuation improved by $1/K(s)$ and reduce the maximum value of $1/K(s)$, but the enhancement at low frequencies is weaker. It is obvious that the parameter design of $Q(s)$ filter is challenging due to the paradox between the closed-loop performance and stability. The third-order low-pass filter $Q_3(s)$ is the preferable implementation of (28) in terms of low-frequency attenuation and stability, as expressed below.

$$Q_3(s)=\frac{3\varsigma s+1}{(\varsigma s+1)^3} \tag{32}$$

To compare the contribution of the simple first-order low-pass filter $Q_1(s)=\frac{1}{\varsigma s+1}$ and the $Q_3(s)$ filter, we have

$$U=\frac{1-Q_1(s)e^{-\tau s}}{1-Q_3(s)e^{-\tau s}} \tag{33}$$

The time delay $e^{-\tau s}$ can be approximated as $e^{-\tau s}=\frac{1}{\tau s+1}$ when $\tau\le 1$. Rewriting (33) as follows:

$$U=\frac{1-\left[(3\varsigma s+1)/(\varsigma s+1)^3\right]\left[1/(\tau s+1)\right]}{1-\left[1/(\varsigma s+1)\right]\left[1/(\tau s+1)\right]} \tag{34}$$

In general, we only focus on the improvement at low frequencies, which implies $s=jw$ and $w\to 0$. Neglecting the high-order terms of $s(jw)$ to simplify the above equation, we have

$$U\approx\lim_{w\to 0}\frac{\tau s\left[(\tau+\varsigma)s+1\right]}{\left[(3\varsigma+\tau)s+1\right]\left[(\tau+\varsigma)s\right]}\approx\frac{\tau}{\tau+\varsigma} \tag{35}$$

It is obvious that $\frac{\tau}{\tau+\varsigma}<1$, which indicates that the third-order low-pass filter $Q_3(s)$ has an extra bonus for the closed-loop performance in comparison with the simple filter $Q_1(s)$. Combining $w_c=\frac{\pi}{4\tau}$ and (30), the roubst stability of the control system based on error-based observation requires $\varsigma>0$ for $m=1$ and $\varsigma>2.2054\tau$ for $m=3$, which restricts the bandwidth of the low-pass filter.

IV. Simulation and Analysis

The time delay T is 0.04 s (two times the CCD sampling time). Thus $K=\frac{\pi}{0.16}$ results in $C_{ttm}(s)=\frac{\pi}{0.16s}$. The Stewart platform with vibration isolation capability can be regarded as a low-pass filter, and the cutoff frequency is about 1.5 Hz. Following the criteria of $GM\geqslant 6$ dB and $PM\gg 45°$, controllers $C_{Ste1}(s)$ and $C_{Ste2}(s)$ can be designed as $C_{Ste1}(s)=C_{Ste2}(s)=(0.37s+4)/s$. According to the model parameters, the open-loop nominal response of the tip-tilt mirror is $G_{ttm}(s)=\frac{0.88}{(0.0009095s+1)(1.013e{-}07s^2+0.000573s+1)}$ [11]. Thus, the amplitude frequency responses of the Stewart platform and tip-tilt mirror control subsystems are shown in Fig. 6. The blue curve represents the open-loop response of the tip-tilt mirror. From Fig. 6, $\frac{w_{of}}{w_f}=61.25$ and $\frac{w_f}{w_c}=25.4$ can be obtained, satisfying (10) and (15). Obviously, the estimation of the control model $\hat{G}_{ttm}(jw)$ can be regarded as 1, and the model-following offloading strategy can be effectively applied to the dual-stage image stabilization system consisting of Stewart platform and tip-tilt mirror.

Substituting $\varsigma=0.2$ and $\tau=0.04$ into (31) yields Fig. 7, which shows the Bode responses of $1/K(s)$ with $m=1$ and $m=3$. According to (35), we have

$$U=\frac{\tau}{\tau+\varsigma}=\frac{0.04}{0.04+0.2}=-15dB \tag{36}$$

which shows agreement with the simulation results described in Fig. 7. From Fig. 7, the term 1/K(s) enhances the error

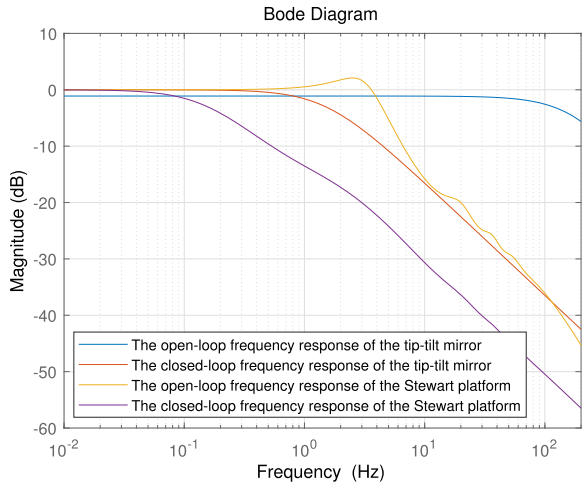

Fig. 6. The amplitude frequency responses of the Stewart platform and tip-tilt mirror control subsystems.

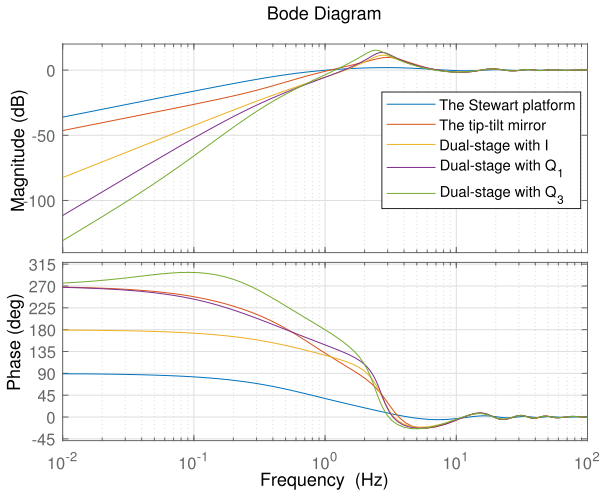

Fig. 8. The Bode responses of the error attenuation function in different situations for the dual-stage system.

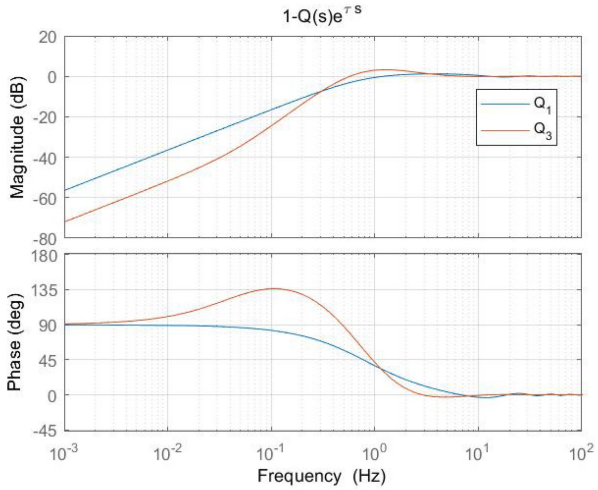

Fig. 7. The Bode responses of $1/K(s)$ with $m = 1$ and $m = 3$.

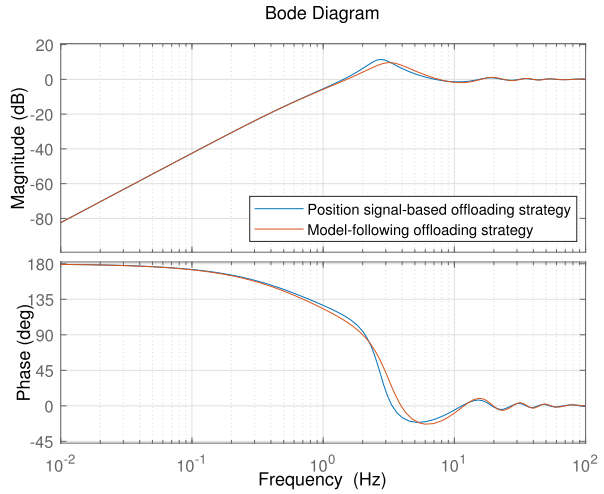

Fig. 9. The Bode responses of the error attenuation function with different offloading strategies.

attenuation by more than -10 dB below the frequency of 0.2 Hz, and compared to the first-order filter $Q_1(s)$, the third-order filter $Q_3(s)$ further enlarges the attenuation by -15 dB below the frequency of 0.03 Hz.

The Bode responses of the error attenuation function in different situations are shown in Fig. 8. The blue line represents the Bode response of the error attenuation function in the Stewart platform control subsystem. It is apparent that the dual-stage control system has a significant improvement on error attenuation in comparison with the single-stage control system. Furthermore, compared with the original feedback loop, the proposed error-based observation control method can effectively enhance the closed-loop performance. Moreover, the third-order low-pass filter $Q_3(s)$ provides an extra bonus in performance compared to the simple filter $Q_1(s)$. Additionally, Fig. 9 compared the traditional position signal-based offloading strategy with the proposed model-following offloading strategy, and the results indicate that both strategies exhibit the same error attenuation capabilities, consistent with (8).

V. Experimental Verification

To verify the effectiveness of the presented approach, an experimental setup implementing the dual-stage image stabilization shown in Fig. 5 is built in Fig. 10. The light source is used to simulate the target. The CCD and the tip-tilt mirror are mounted on the cubic Stewart platform. The CCD detects the light spot and provides the LOS error through the image processing system. The tip-tilt mirror has a small stroke range of $\pm$1mrad. However, the Stewart platform features a larger stroke range at $\pm$15.4625mrad. Additionally, the CCD has a sampling rate of 50 Hz, and the working frequency of the dual-stage system is 10 KHz. Note that this article only presents the experimental results of azimuth axis due to the similarity.

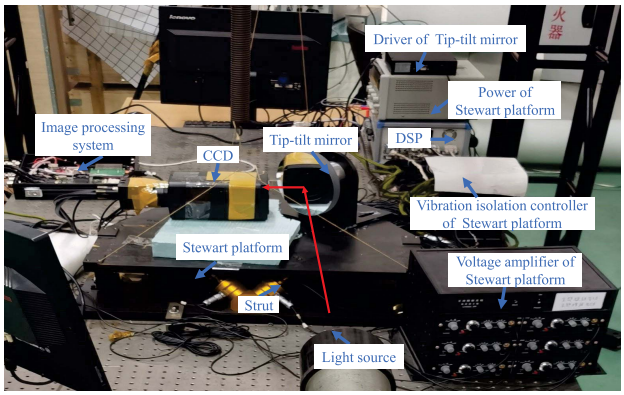

Fig. 10. Experimental setup.

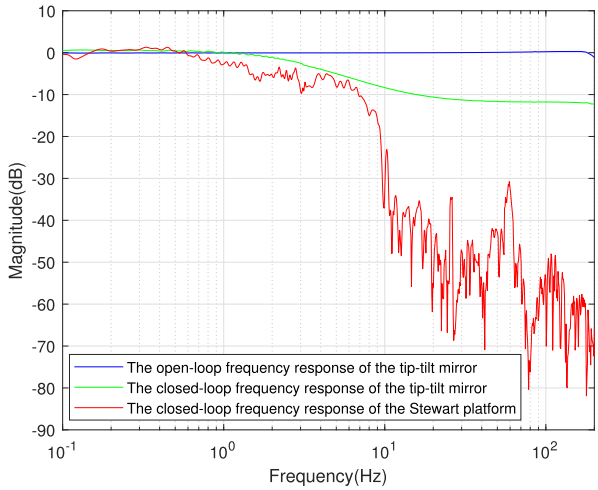

Fig. 11. The amplitude frequency responses in different situations for the dual-stage system.

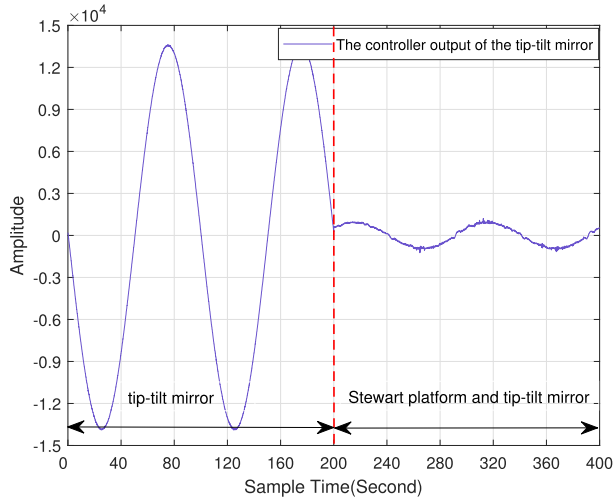

Fig. 12. The controller output of the tip-tilt mirror before and after offloading.

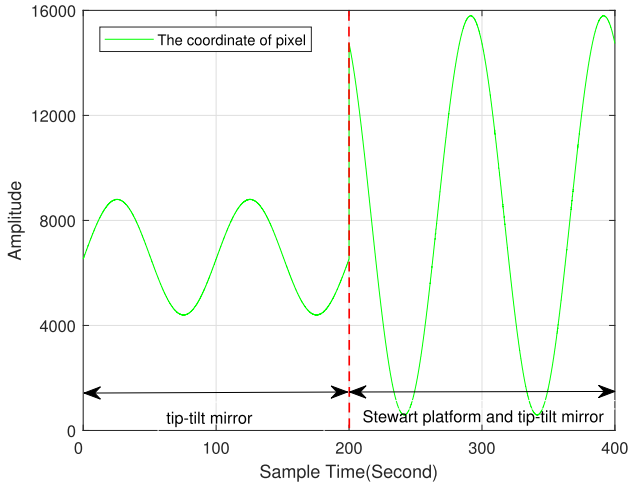

Fig. 13. The maximum tracking angle before and after offloading.

A. The Model-Following Offloading Strategy

To validate (10) and (15), the amplitude frequency responses in different situations for the dual-stage system are depicted in Fig. 11. The red curve represents the amplitude frequency response of the Stewart platform with vibration isolation capability, indicating that the bandwidth of the Stewart platform is 1.07 Hz. The cut-off frequency of the tip-tilt mirror is 241 Hz, and the closed-loop bandwidth of the tip-tilt mirror control subsystem is 3.5 Hz. Thus, $\frac{w_f}{w_c} \gg 1$ and $\frac{w_{of}}{w_f} \geqslant 1$, satisfying (10) and (15), with condition (16) also being met. As a result, the model-following offloading strategy can be employed in this dual-stage system.

The target trajectory $R(s)$ is a sinusoidal signal $\theta = A \times \sin(2\pi ft)$ with amplitude A and frequency f. Let the sinusoidal trajectory be $\theta = (0.9499 \times \sin(2 \times \pi \times 0.01 \times t))(mrad)$, Fig. 13 illustrates the controller output of the tip-tilt mirror before and after offloading. Clearly, compared to the case without offloading, the controller output decreases by 92.6% when the tip-tilt mirror is offloaded onto the Stewart platform, indicating that the offloading control is achieved. Besides, Fig. 13 shows the maximum tracking angle before and after offloading, represented by the pixel coordinates. The maximum angle before offloading is ± 0.9499mrad, and it can be increased to ± 3.2815mrad when the offloading control is implemented.Therefore, the offloading control can increase the tracking range of the system.

B. The Model-Following Dual-Stage Tracking Control

The experiment is to validate the effectiveness of the dual-stage control system in improving tracking accuracy. The amplitude of the tracking signal A is 0.9499mrad, and the frequencies of the tracking signal f are 0.01 Hz, 0.03 Hz, 0.05 Hz, 0.08 Hz, and 0.1 Hz, respectively. The resulting errors with the Stewart platform subsystem, tip-tilt mirror subsystem, and the dual-stage system are demonstrated in Fig. 14. The blue curve represents the resulting error only using the Stewart platform subsystem. It can be seen from Fig. 14 that the dual-stage system has better error attenuation capability compared with the single-stage system below 0.1 Hz. Thus, the dual-stage system

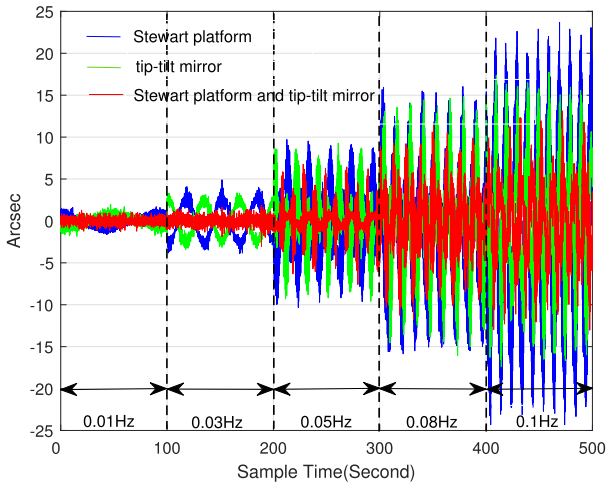

Fig. 14. The resulting errors with the Stewart platform subsystem, tip-tilt mirror subsystem, and the dual-stage system.

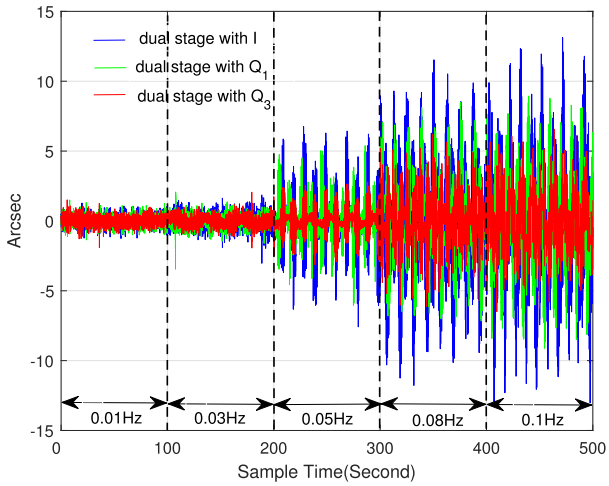

Fig. 16. The resulting errors of classical feedback control and error-based observation control with $Q_1(s)$ and $Q_3(s)$ for the dual-stage system.

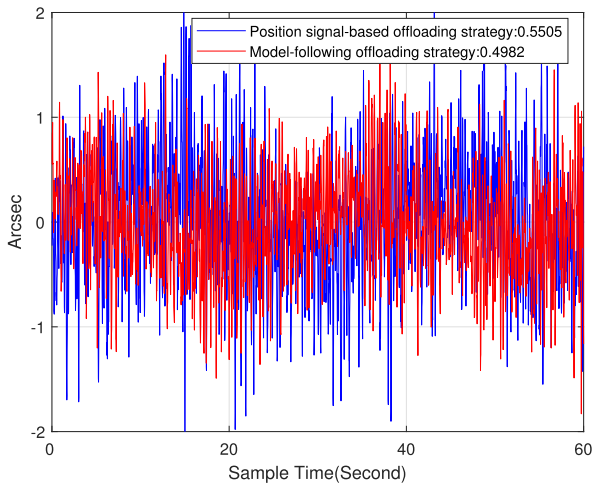

Fig. 15. The resulting errors with two offloading strategies.

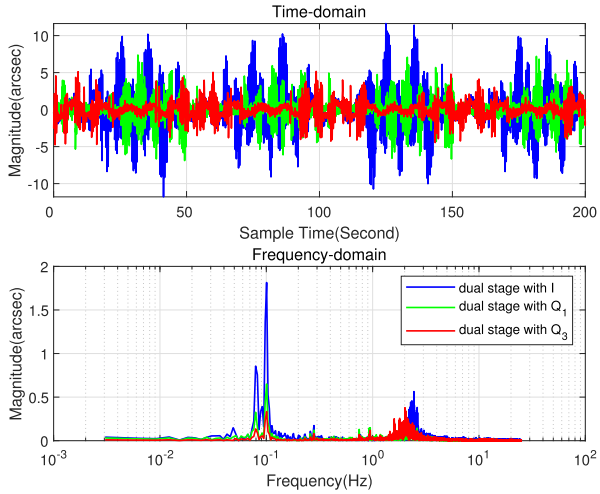

Fig. 17. A comparison of the resulting errors in the time domain and frequency domain when using classical feedback control and error-based observation control with $Q_1(s)$ and $Q_3(s)$.

proves to be effective in enhancing tracking precision. Besides, to validate the superiority of the proposed offloading strategy over the traditional one in improving accuracy, strain gauge sensors (SGS) are utilized to measure the position signal of the Tip-tilt mirror, where temperature-induced zero drift may introduce measurement errors. Let the sinusoidal trajectory be $\theta = (0.9499 \times \sin(2 \times \pi \times 0.01 \times t))(mrad)$. The resulting errors of the traditional and proposed offloading strategies are shown in Fig. 15, with RMS errors of 0.5505mrad and 0.4982mrad respectively. Obviously, the proposed method achieves higher tracking accuracy.

C. The Error-Based Observation Control

The experiment aims to validate the improvement in closed-loop performance introduced by the error-based observation control. In order to facilitate a better comparison, the tracking trajectory is kept the same as in Section V-B. Fig. 16 shows the resulting errors of classical feedback control and error-based observation control with $Q_1(s)$ and $Q_3(s)$. The blue curve represents the resulting error using classical feedback control with an integral controller. It is evident that the error-based observation control method exhibits significant improvement below 0.1 Hz compared to the classical feedback control. Moreover, the third-order filter Q_3 is more efficient than the first-order filter Q_1. Additionally, let the target trajectory be a mixed-frequency signal $\theta = (0.22 \times \sin(2 \times \pi \times 0.01 \times t) + 0.22 \times \sin(2 \times \pi \times 0.03 \times t) + 0.22 \times \sin(2 \times \pi \times 0.05 \times t) + 0.44 \times \sin(2 \times \pi \times 0.08 \times t) + 0.44 \times \sin(2 \times \pi \times 0.1 \times t))(mrad)$. Fig. 17 presents a comparison of the resulting errors in the time domain and frequency domain when using classical feedback control and error-based observation control with $Q_1(s)$ and $Q_3(s)$, which further confirms the efficacy of the error-based observation control method.

The root-mean-square (RMS) errors of Figs. 14 and 16 are listed in Table I. Table I indicates that at 0.01 Hz, the error

TABLE I
THE RMS ERRORS

Tracking frequency (Hz)	RMS of arcsec (")				
	Stewart platform	Tip-tilt mirror	Dual stage with I	Dual stage with Q_1	Dual stage with Q_3
0.01	0.7134	0.6383	0.3332	0.3255	0.3156
0.03	1.9457	1.6956	0.4929	0.3945	0.3417
0.05	3.9174	3.3076	1.4823	0.9875	0.6908
0.08	7.5626	5.6041	3.2416	2.2901	1.5810
0.10	11.9820	6.8217	3.9842	2.8820	1.8620

attenuation of the dual-stage system using classical feedback control has reached its limit, and there is no significant improvement with the error-based observation control. However, in the frequency range from 0.03 Hz to 0.1 Hz, error-based observation control exhibits enhanced error attenuation compared to traditional feedback control. Additionally, the error-based observation with $Q_3(s)$ shows extra improvement compared to the error-based observation with $Q_1(s)$.

D. Discussion of Experimental Results

To validate the effectiveness of the model-following offloading control strategy proposed, three experiments were conducted. In the subsection A, the experimental results demonstrated that the constructed dual-stage system satisfies decoupling conditions $\frac{w_{of}}{w_f} \gg 1$ and $\frac{w_f}{w_c} \gg 1$. Additionally, after offloading, the working range increased from 0.9499mrad to 3.28mrad. In the subsection B, the dual-stage control system's ability to enhance tracking accuracy is verified. When the target motion frequency is between 0.01 and 0.1 Hz, compared to using only the Stewart platform, the error attenuation rate under dual-level control exceeds 53%. In the subsection C, the experiment was conducted to validate the effectiveness of the error-based observation control method. The target motion frequency is set the same as in subsection B. Compared with PI controller, the error-based observation control method can improve the tracking accuracy, and the $Q_3(s)$ filter has a better enhancement compared to $Q_1(s)$ filter. However, when the frequency is 0.01 Hz, the RMS of the closed-loop errors under different situations is essentially equal. This is because of system noise, and error attenuation has reached its limit. However, the proposed model-following offloading strategy has certain limitations. The closed-loop bandwidth of the fine stage must be significantly greater than that of the coarse stage. Otherwise, equation $L_c(s) = L_c{}'(s)$ does not hold, and system stability cannot be ensured when both the fine and coarse stages are individually stable.

VI. CONCLUSION

This article develops a dual-stage image stabilization system based on the model-following offloading strategy to improve the tracking performance for space optical payloads. We compared the conventional position signal-based offloading strategy with the model-following offloading strategy. It is evident that the improved model-following offloading strategy, by utilizing model-based estimation, not only reduces the difficulty of system decoupling but also eliminates the requirement for additional position sensors. Furthermore, a novel CCD-based control scheme is devised to solve the coupling issue of tracking control for the Stewart platform subsystem, and an error-based observation control method is presented to compensate the time delay of the CCD for the tip-tilt subsystem. In the error-based observation method, due to being plugged into the original feedback control loop, a high gain to the control system can be achieved by optimizing the Q-filter. We focused on the implementation of the error-based observation control method, the analysis of stability, and the parameter design of the Q-filter. Although the control bandwidth is not expanded with this method, the error attenuation at low frequencies is enhanced. The experimental results of the dual-stage image stabilization system demonstrate the effectiveness of the presented approach. Due to a straightforward structure and implementation, this method can be extended to other high-performance servo control systems that rely solely on position error. In the following work, we will explore the parallel filter to optimize the Q-filter.

Disclosures

The authors declare that there are no conflicts of interest related to this article.

Data Availability Statement

The data that support the findings of this study are available upon reasonable request from the corresponding author.

REFERENCES

[1] N. Pedreiro, "Next generation space telescope pointing stability," in *Proc. AIAA Guid., Navigation, Control Conf. Exhibit*, 2000.
[2] C. Liu, X. Jing, S. Daley, and F. Li, "Recent advances in micro-vibration isolation," *Mech. Syst. Signal Process.*, vol. 56, pp. 55–80, 2015.
[3] M. Furqan, M. Suhaib, and N. Ahmad, "Studies on stewart platform manipulator: A review," *J. Mech. Sci. Technol.*, vol. 31, pp. 4459–4470, 2017.
[4] E. M. Flint, P. Flannery, M. E. Evert, and E. H. Anderson, "Cryocooler disturbance reduction with single and multiple axis active/passive vibration control systems," in *Proc. Smart Structures Mater., Damping Isolation*, 2000, pp. 487–498.
[5] A. A. Hanieh, "Active isolation and damping of vibrations via stewart platform," Ph.D. dissertation, Université Libre de Bruxelles, Active Structures Laboratory, 2003.
[6] M. B. McMickell, T. Kreider, E. Hansen, T. Davis, and M. Gonzalez, "Optical payload isolation using the miniature vibration isolation system (MVIS-II)," in *Proc. Ind. Commercial Appl. Smart Structures Technol.*, 2007, pp. 14–26.
[7] Y. Zhang and X. Guan, "Active damping control of flexible appendages for spacecraft," *Aerosp. Sci. Technol.*, vol. 75, pp. 237–244, 2018.
[8] D. Thayer, M. Campbell, J. Vagners, and A. V. Flotow, "Six-axis vibration isolation system using soft actuators and multiple sensors," *J. Spacecraft Rockets*, vol. 39, no. 2, pp. 206–212, 2002.
[9] C. Wang, X. Xie, Y. Chen, and Z. Zhang, "Investigation on active vibration isolation of a stewart platform with piezoelectric actuators," *J. Sound Vib.*, vol. 383, pp. 1–19, 2016.
[10] T. Tao et al., "A review on precision control methodologies for optical electric tracking control system," *Opto- Electron. Eng.*, vol. 47, no. 10, pp. 1–29, 2020.
[11] Q. Li, L. Liu, and S. Tang, "Composite axis control system development of airborne electro-optical platform," in *Proc. IEEE Int. Conf. Cybern. Intell. Syst. IEEE Conf. Robot., Automat. Mechatron.*, 2017, pp. 399–404.
[12] P. Liu et al., "Research on key technology of compound axis control of periscope optical communication terminal," in *Proc. IEEE 6th Inf. Technol. Mechatron. Eng. Conf.*, 2022, pp. 939–942.

[13] S. Xu and J. Han, "Design and analysis of ATP compound axis control system for intersatellite optical communication," in *Proc. IEEE 4th Int. Conf. Control Sci. Syst. Eng.*, 2018, pp. 312–316.
[14] P. Brugarolas et al., "ACCESS pointing control system," in *Proc. Space Telescopes Instrum., Opt., Infrared, Millimeter Wave*, 2010, pp. 1661–1682.
[15] H. Yun, L. Liu, Q. Li, and H. Yang, "Investigation on two-stage vibration suppression and precision pointing for space optical payloads," *Aerosp. Sci. Technol.*, vol. 96, 2020, Art. no. 105543.
[16] Z. Liangzong, Y. Tao, W. Yun, and T. Tao, "Image measurement-based two-stage control of stewart platform," *Opto- Electron. Eng.*, vol. 49, no. 8, pp. 1–10, 2022.
[17] J. Hilkert, "Inertially stabilized platform technology concepts and principles," *IEEE Control Syst. Mag.*, vol. 28, no. 1, pp. 26–46, Feb. 2008.
[18] M. Boerlage, M. Steinbuch, P. Lambrechts, and M. v. d. Wal, "Model-based feedforward for motion systems," in *Proc. IEEE Conf. Control Appl.*, 2003, pp. 1158–1163.
[19] M. Boerlage, R. Tousain, and M. Steinbuch, "Jerk derivative feedforward control for motion systems," in *Proc. IEEE Amer. control Conf.*, 2004, pp. 4843–4848.
[20] Y. Yuan, Z. Wang, and L. Guo, "Event-triggered strategy design for discrete-time nonlinear quadratic games with disturbance compensations: The noncooperative case," *IEEE Trans. Syst., Man, Cybern. Syst.*, vol. 48, no. 11, pp. 1885–1896, Nov. 2018.
[21] T. Tang, H. Cai, Y. Huang, and G. Ren, "Combined line-of-sight error and angular position to generate feedforward control for a charge-coupled device–based tracking loop," *Opt. Eng.*, vol. 54, no. 10, pp. 105107–105107, 2015.
[22] R. Stanciu and P. Y. Oh, "Feedforward control for human-in-the-loop camera systems," in *Proc. IEEE Int. Conf. Robot. Automat.*, 2004, pp. 1–6.
[23] P. Corke and M. Good, "Controller design for high-performance visual servoing," *IFAC Proc. Volumes*, vol. 26, no. 2, pp. 629–632, 1993.
[24] J. Hilkert, "Kinematic algorithms for line-of-sight pointing and scanning using INS/GPS position and velocity information," in *Proc. Acquisition, Tracking, Pointing XIX*, 2005, pp. 11–22.
[25] N. F. Palumbo, R. A. Blauwkamp, and J. M. Lloyd, "Basic principles of homing guidance," *Johns Hopkins APL Tech. Dig.*, vol. 29, no. 1, pp. 25–41, 2010.
[26] Z. Hurák and M. Řezáč, "Delay compensation in a dual-rate cascade visual servomechanism," in *Proc. IEEE 49th Conf. Decis. Control*, 2010, pp. 1639–1643.
[27] H. Yun, L. Liu, Q. Li, W. Li, and L. Tang, "Development of an isotropic stewart platform for telescope secondary mirror," *Mech. Syst. Signal Process.*, vol. 127, pp. 328–344, 2019.
[28] W. Chen et al., "Dynamics modeling and modal space control strategy of ship-borne stewart platform for wave compensation," *J. Mechanisms Robot.*, vol. 15, no. 4, 2023, Art. no. 041015.
[29] X. Chen and M. Tomizuka, "New repetitive control with improved steady-state performance and accelerated transient," *IEEE Trans. Control Syst. Technol.*, vol. 22, no. 2, pp. 664–675, Mar. 2014.
[30] Y. Wu, L. Zhang, T. Xu, and T. Tang, "Enhanced observer control of a cubic Stewart platform with image sensor measurement," *IEEE Photon. J.*, vol. 14, no. 5, pp. 1–8, Oct. 2022.